

VLTI observations of the Orion Belt stars: I. ε Orionis \star

A. Oplštilová¹, M. Brož¹, C. A. Hummel², P. Harmanec¹, and B. N. Barlow³

¹ Charles University, Faculty of Mathematics and Physics, Astronomical Institute, V Holešovičkách 2, CZ-180 00 Praha 8-Trója, Czech Republic

² European Southern Observatory, Karl-Schwarzschild-Str. 2, D-85748 Garching, Germany

³ Department of Physics and Astronomy, University of North Carolina at Chapel Hill, Chapel Hill, NC 27599, USA

Received July 4, 2025

ABSTRACT

Context. Massive stars play a decisive role in the evolution of the Universe. They are the primary sources of ionising radiation, generate strong stellar winds affecting the interstellar medium, and ultimately end their lives as supernovae, ejecting synthesised, r-process elements.

Aims. In order to constrain their current state and structure, we need sufficiently complex models, constrained by astrometric, interferometric, and spectroscopic observations. However, they are not available for distant stars. Instead, we focused on the nearest massive stars in the Orion Belt.

Methods. We obtained VLTI interferometric observations of Orion Belt stars and calibrated visibility data from the GRAVITY and PIONIER instruments. Additionally, we obtained spectroscopic data from the CFHT and CTIO observatories. For modelling, we used a modified version of PHOEBE2, extended with new interferometric and spectroscopic modules. To describe non-spherical, rotating, or Roche-like stars, integrals over triangular meshes have to be computed, using extensive grids of synthetic spectra (OSTAR, BSTAR, ATLAS). For fitting, we used the simplex algorithm and χ^2 mapping of the parameter space.

Results. In this paper, the first in a series, we present single-star models of the B0 Ia supergiant ε Ori. Interferometric visibilities indicate that the star is not spherical but rotating close to its critical velocity. The preferred distance, $d = (384 \pm 8)$ pc, corresponds to the median of distances for the Orion OB1b association. Specifically, we obtained the following parameters: mass $m = (28.4 \pm 2.0) M_{\odot}$, equivalent radius $R = (27.6 \pm 1.5) R_{\odot}$ (the polar and equatorial values were $22.3 R_{\odot}$ and $33.6 R_{\odot}$, respectively), effective temperature $T_{\text{eff}} \approx 25\,000$ K, inclination of the rotation axis $i \approx 45$ deg, longitude of the ascending node (of the equator), $\Omega \approx 300$ deg, and period $P_{\text{rot}} = 4.3^{+1.0}_{-0.0}$ d. This ‘compromise’ model provides a reasonable fit to wind-free Balmer line profiles (H γ , H δ , H ε , etc.), but there is still some tension between interferometric and spectroscopic datasets, corresponding to a faster- vs. slower-rotating star.

Conclusions. Our fast-rotating model implies that circumstellar matter should be naturally present, in the form of wind or disk, and contributing to continuum radiation. The fast rotation of ε Ori is compatible with a merger, formed from a multiple system of comparable mass, like δ , ζ , or σ Ori.

Key words. Stars: massive – Techniques: interferometric – Stars: individual: ε Ori – Stars: individual: Orion’s Belt

1. OB stars in the Orion Belt

OB stars live relatively short—only a few millions or tens of millions of years, yet they are crucial cosmic engines with influence on the Universe that outlasts their lifetimes. They exert strong feedback on their environment; not only as sources of energy, ionising photons, chemical elements—through winds or core-collapse supernovae explosions (Clayton 1983)—but also as precursors of neutron stars, black holes, and consequently gravitational wave sources (Marchant et al. 2021).

Most likely precursors include overcontact binaries (Almeida et al. 2015), X-ray binaries (Atri et al. 2019), quiescent binaries (Shenar et al. 2022), or pair-instability supernovae (Renzo et al. 2022). Various formation channels must be constrained by photonic observations. The distribution of black hole masses (Abbott et al. 2021) indicates a hierarchical merging. This is complicated by “kicks” of the order of 100 km/s, during explosions (Wongwathanarat et al. 2013) or mergers (Shenar et al. 2022). The kicks can be compensated by the escape veloc-

ity from nuclear clusters or the escape velocity from multiple systems, where the radial velocities (RVs) of components are comparable to the kick velocities.

The very characteristic of massive stars is multiplicity; 90% of massive hot OB stars possess at least one stellar companion (Sana et al. 2014; Sota et al. 2014; Maíz Apellániz et al. 2019; Pauwels et al. 2023), which influences their evolution throughout their lives. Yet, some stars remain single (e.g. ε Ori), even though they share the same birth environment with multiple systems. Considering the possible interactions among stars, they might be the result of a more complicated evolutionary process, including mass transfer or mergers resulting from close encounters between stars.

The evolution of massive stars still remains poorly constrained by observations. The primary kind of observation constraining diameters is long-baseline interferometry. While the most massive stars in the Large Magellanic Cloud, e.g. BAT99-98 with $M \approx 200 M_{\odot}$ located in the Tarantula nebula (30 Dor) (Hainich et al. 2014; Kalari et al. 2022), are too distant (50 kpc) for interferometric measurements, the Orion OB1 association at about 400 pc from us seems to be a perfect region for the inves-

Send offprint requests to: A.O.,

e-mail: alzbeta.oplistilova@gmail.com

* Based on ESO proposal Programme ID: 112.25JX, PI A. Oplštilová

tigation of questions related to the birth of OB stars and their evolution.

The brightest stars in the Orion Belt, members of the OB1b Orion association, δ Ori, ζ Ori, σ Ori, and ε Ori with individual component masses of up to $35 M_{\odot}$ (Hummel et al. 2013; Schaefer et al. 2016a; Puebla et al. 2016a; Oplištilová et al. 2023) represent massive stars that are accessible to the most advanced optical interferometers. The parallaxes of faint stars surrounding the aforementioned bright stars were measured in Gaia DR3 (Gaia Collaboration et al. 2021); the corresponding distances are all around 0.38 kpc (Oplištilová et al. 2023). It is thus possible to measure their angular separations and angular diameters.

In this first paper, we focus on ε Ori (Alnilam, 46 Ori, HD 37128), which is the largest and brightest star in the Orion Belt. Based on photometric measurements taken at the Hvar Observatory (Božić & Harmanec 2023), its standard magnitudes are: $V = 1.691$ mag, $B = 1.509$ mag, and $U = 0.495$ mag. It is classified as a B0 Ia blue supergiant and represents the only massive single star in Orion's Belt. Its mass of about $30 M_{\odot}$ (Puebla et al. 2016a) is similar to the total masses of the other multiple systems in Orion. Also, it has an intense wind (Puebla et al. 2016a) and a mass-loss rate of up to $\dot{M} = 5.25 \cdot 10^{-6} M_{\odot} \text{ yr}^{-1}$ (Repolust et al. 2005). It might be the case that ε Ori is a post-mass-transfer object, and represents a future evolved state of multiple stellar systems in Orion. For this reason, we include a brief discussion of the relevant systems, δ , ζ , and σ Ori, to enable comparison of their masses, radii, spectral types, etc.

δ Ori (Mintaka, HD 36486, HR 1852/1851) is our closest massive multiple system consisting of five components in total: [(Aa1 + Aa2) + Ab] + (Ca + Cb). The triple star A (O9.5 II + B2 V + B0 IV) has the periods $P_1 = 5.732436$ d, $P_2 = 55450$ d and the mass $17.8 + 8.5 + 8.7 \approx 35 M_{\odot}$ (Oplištilová et al. 2023). The primary (Aa1) is an unusually evolved O-type star. The star has been studied in a series of papers by Corcoran et al. (2015), Pablo et al. (2015), Nichols et al. (2015), and Shenar et al. (2015). We have already constructed a model of δ Ori A (Oplištilová et al. 2023), based on diverse observational data (photometry, astrometry, radial velocities, eclipse timings, eclipse duration, spectral line profiles, and spectral-energy distribution), with the exception of interferometry, as previous VLTI/AMBER data were not usable. One conclusion from that study was that the compact binary Aa1+Aa2 is a pre-mass-transfer object, while the tertiary seems to be unusually inflated (according to its $\log g$ and the HR diagram).

ζ Ori (Alnitak, 50 Ori, HR 1948/1949) consists of four components [(Aa + Ab) + B] + C, also includes a triple star O9.7 Ib + B0.5 IV + B0 III and, in particular, a double-lined spectroscopic binary with the mass $33 + 14 \approx 47 M_{\odot}$ (Hummel et al. 2000). The 2 mag fainter companion Ab with the period $P_1 \approx 2687$ d, mean separation of 45 mas, and eccentricity $e_1 = 0.338$ was discovered by Hummel et al. (2000). The primary Aa is the only known magnetic O-type supergiant. Tertiary B has a fast rotation of 350 km/s, separation of 2.4 arcsec, period $P_2 = 1509$ yr, and eccentricity $e_2 = 0.07$.

Finally, σ Ori (48 Ori, HD 37468, HR 1931) has six components [(Aa + Ab) + B] + C + D + E of spectral types [(O9.5 V + B0.5 V) + A2V] + B2V + B2V + ?. The triple star has masses of $17 + 13 + 12 \approx 42 M_{\odot}$. Binary A ($P_1 \approx 143$ d) and component B form a visual pair with $P_2 \approx 160$ yr. The angular separations of all components are 4.3 mas, 260 mas, 11 arcsec, 13 arcsec, and 42 arcsec, respectively. Unlike δ Ori, the inner orbit of σ Ori is eccentric, while the outer is circular (Schaefer et al. 2016b). According to Schaefer et al. (2016b), the expected angular diameters are 0.27 and 0.21 mas for Aa and Ab, respec-

tively. The system has already been observed by interferometers such as CHARA/MIRC, NPOI, and VLTI/AMBER; however, the diameters were unresolved.

In 2023, we succeeded with the ESO proposal (Programme ID: 112.25JX) to observe ε , δ , ζ , and σ Ori with the Very Large Telescope Interferometer (VLTI). The main goal was to resolve the angular diameters of individual components to constrain complex models of the stellar systems.

2. Observational data

Hereinafter, we describe the observational datasets, including interferometry from VLTI instruments, spectroscopy from CFHT and CTIO, together with other datasets used for modelling ε Ori.

2.0. VLTI/GRAVITY interferometry

In our two runs of Programme ID: 112.25JX, (PI A. Oplištilová, 12 h + 1 h) – in phase 112, running between 1/10/23 and 31/3/24 at Cerro Paranal in northern Chile, we obtained observations of ζ , σ , and δ Ori with the GRAVITY instrument (Eisenhauer et al. 2011; GRAVITY Collaboration et al. 2017) and observations of ε Ori with the PIONIER instrument (Le Bouquin et al. 2011).

Both runs were performed in service mode. Such data should enable us to fit stars' angular diameters and angular positions with up to 10-microarcsecond accuracy.

For observations with GRAVITY, we requested 12 concatenations, each including 2 observing blocks (OBs), science target and calibrator (CAL-SCI). Each concatenation lasted 1 h; thus, we obtained observations on four different nights for each target, 12 hours of observations in total. We chose the extended configuration, which made these observations possible for the first time, and the high spectrometer resolution. The observations (snapshots) were in on-axis mode, with automatic fringe tracking, adaptive optics with Coude guiding, and standard calibration. For δ and σ Ori, we set the Wollaston spectrometer out and for ζ Ori, in. Otherwise, the brightest object ζ Ori would be saturated. All our three targets were very bright; therefore, we used the auxiliary telescopes (ATs) and allowed for the worst weather conditions when observations are possible, which were a seeing < 1.4 arcsecs, variable sky with thin cirrus, and an air mass of 1.6.

We performed the calibration using the EsoReflex GRAVITY pipeline (Freudling et al. 2013). The essence of calibration is to compare the visibilities of calibrators (see Table 1) with the theoretical visibilities of a uniform disk, which is described by

$$\mu(u, v) = \frac{2 J_1(\pi \theta \sqrt{u^2 + v^2})}{\pi \theta \sqrt{u^2 + v^2}}, \quad (1)$$

where J_1 is the Bessel function of the first order, the square root $\sqrt{u^2 + v^2}$ corresponds to the length of a baseline, and θ is the angular diameter of a star. The visibility function for a uniform disk is the simplest model, but it is sufficient for the calibration process. The larger the diameter, the faster the visibility drops. The comparison of theoretical and observed visibilities is expressed by a transfer function as the ratio of the calibrator's squared visibilities and theoretical squared visibilities for a uniform disk

$$\text{TF} = \frac{V_{\text{cal}}^2}{V_{\text{UD}}^2} \quad (2)$$

The transfer function is used to reduce raw uncalibrated data; the reduced data V_{*}^2 are the ratio of raw data and the transfer function

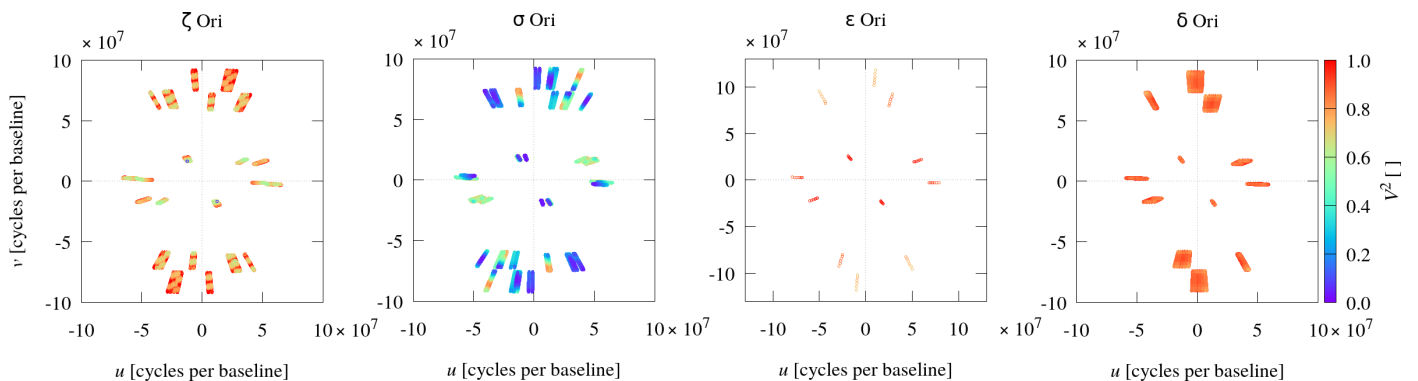


Fig. 1. Coverage for interferometric measurements showing the squared visibility V^2 vs. baselines $(u, v) \equiv \mathbf{B}/\lambda$ in cycles per baseline. Individual panels show four stars in Orion’s Belt (ζ , σ , ϵ , and δ Ori). For each star, all nights are plotted. Colours correspond to visibility values.

$$V_*^2 = \frac{V_{\text{raw}}^2}{\text{TF}}. \quad (3)$$

For all three objects, we obtained squared visibilities measured on six baselines, covering the wavelength range from $1.95 \mu\text{m}$ to $2.45 \mu\text{m}$. The coverage of measurements in uv -planes for each target is shown in Fig. 1, and examples of reduced squared visibilities V^2 and the corresponding calibrators’ visibilities are in Fig. 2. We also obtained closure phases for four triangles composed of those six baselines. We checked the closure phases of calibrators; they were close to zero as expected.

In the case of ζ Ori and its calibrator, we obtained two polarisation directions, P_1 and P_2 , thanks to the Wollaston prism. However, since the object does not have a strong magnetic field, we cannot use the polarimetric data to determine any properties. The Wollaston prism was used just to prevent saturation of this bright target.

2.1. VLTI/PIONIER interferometry

With the PIONIER instrument, we proposed a single concatenation composed of three observing blocks (CAL-SCI-CAL) and obtained six interferometric measurements of ϵ Ori on six baselines, within one hour of observing time. This resulted in a total of 36 squared visibility and 24 closure phase measurements. To get this snapshot, we applied for the grism as the disperser for PIONIER. The PIONIER instrument works in the H-band ($1.52\text{--}1.76 \mu\text{m}$), which delivers a better angular resolution than GRAVITY for measuring a single star. The target is very bright; thus, observations could be conducted under relaxed weather constraints: seeing <1.15 arcsec, variable sky with thin cirrus, and an air mass of 2.0. Data reduction was performed using the Pndrs software (Le Bouquin et al. 2011). The uv -plane coverage is shown in Fig. 1, and the reduced squared visibilities V^2 together with those of the calibrator ζ Lep are in Fig. 2.

2.2. CTIO/CHIRON and CFHT Spectroscopy

We obtained four echelle spectra of spectral range (4504–8900) \AA at the Cerro Tololo Inter-American Observatory (CTIO) with the 1.5-m reflector using the highly stable cross-dispersed echelle spectrometer CHIRON. We used the fibre mode with the resolution of $R \approx 25\,000$. A preliminary reduction to 1-D spectra was carried out at CTIO (Tokovinin et al. 2013). We performed

Table 1. Epochs of interferometric observations and uniform-disk diameters (UDD) of calibrators. The values were taken from the VLTI or PIONIER pipelines, or recalibrated by us in the case of ζ Ori.

Star	T [HJD]	Calibrators	UDD_{cal} [mas]
δ Ori	2460268.66081427	HIP 26149	0.6658
	2460270.66197214		
	2460271.64182168		
	2460300.59365039		
ζ Ori	2460269.65275756	HIP 26108	1.9350
	2460271.75297908		
	2460300.67146289		
	2460317.64698373		
σ Ori	2460268.82653117	HIP 26174	0.6419
	2460271.72554332		
	2460317.61074530		
	2460318.55852424		
ϵ Ori	2460268.50080073	ζ Lep	0.7950

rectification using the reSPEF02 software written by A. Harmanec¹.

Additionally, we used four spectra measured by the 3.6-m Canada-France-Hawaii Telescope (CFHT), located near the summit of Mauna Kea on Hawaii. The spectra from the ESPaDOnS instrument cover the region of (3815–6600) \AA and have the resolution of 68 000. These archival spectra have relatively low uncertainties in the normalised intensity, less than 0.01, corresponding to photon noise for bright stars. Due to remaining rectification systematics, we added a value of 0.01 to uncertainties.

2.3. Spectral-energy distribution (SED)

To compute SED, we downloaded absolute fluxes from the photometric catalogues in the Vizier tool (Allen et al. 2014). We selected all measurements within the wavelength range of the BSTAR absolute synthetic spectra. Specifically, we obtained measurements between 0.353 and $2.1 \mu\text{m}$ in the standard Johnson photometric system (Ducati 2002), and measurements from Gaia DR3 (Gaia Collaboration 2020), and 2MASS (Cutri et al. 2003). We omitted clear outliers and multiple entries. For mea-

¹ <https://astro.troja.mff.cuni.cz/projects/respefo>

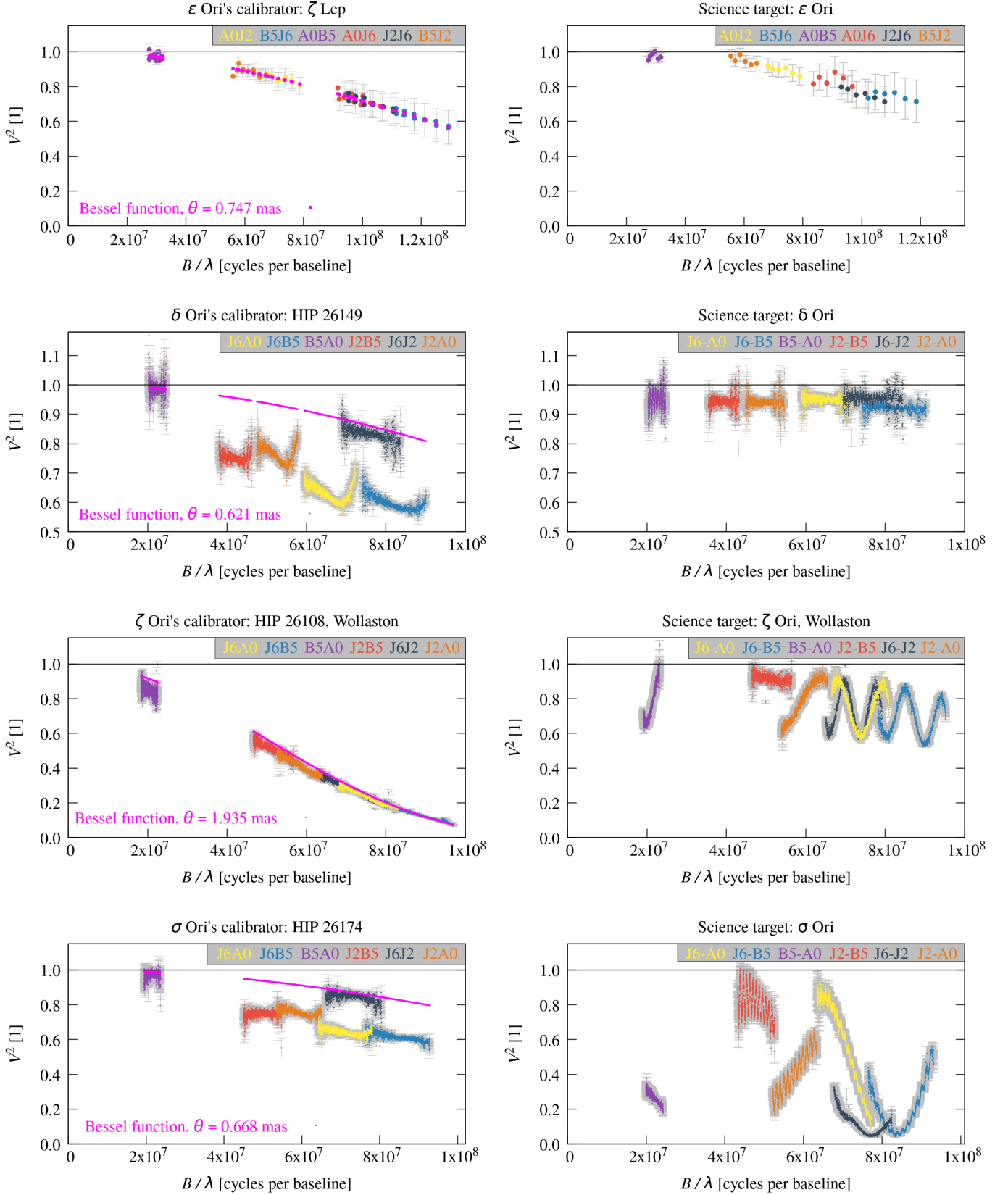


Fig. 2. Examples of raw visibilities of the calibrators and reduced squared visibilities V^2 of the science targets, ϵ , δ , ζ , and σ Ori. Measurements are from nights: 20 November 2023, 22 November 2023, 8 January 2024, 23 November 2023, respectively. Left column: calibrators and the corresponding Bessel functions with the calibrator's diameters plotted for reference (magenta). Right column: science targets with obvious signals from companions. For the single star ϵ Ori, the signal suggests an elongated or non-spherical shape, unlike the calibrator ζ Lep, which exhibits a perfectly spherical shape. Colours correspond to individual baselines.

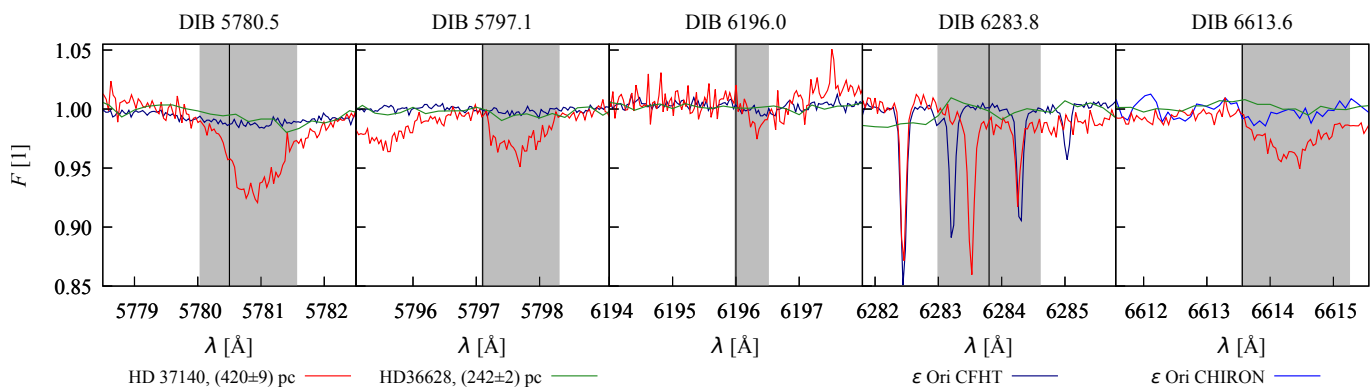


Fig. 3. Comparison of DIBs’ intensities for ϵ Ori and stars which are close on the sky. (HD 37140, and HD 36628). The most distant star has the deepest DIBs, while the star with the lowest distance has very weak DIBs. The spectrum of ϵ Ori also shows weak DIBs, which suggests its distance is lower than 420 pc. The spectra were taken from public archives of CFHT and ESO.

measurements without reported uncertainties, we assumed the value of 0.02 mag. Hipparcos measurements were not used due to underestimated systematic uncertainties. The final dataset contained 13 data points see Table C.1.

To compute the reddening E_{B-V} for ϵ Ori, we used the differential photometry measured in October 2006 and February 2024 (2454015.6–2460362.4 HJD) at the Hvar Observatory (Božić & Harmanec 2023), namely, the observed colour index $(B - V)_0 = -0.192$ mag. For the corresponding spectral type B0Ia, the intrinsic colour is $(B - V) = -0.240$, according to (Golay 1974), consequently, $E_{B-V} = 0.05$ mag and $A_V = 0.155$ mag, which is in agreement with Fan et al. (2017) and negligible in the infrared.

For the construction of SED, we also used calibrated UBVI photometry from the Hvar differential archive. It contains 21 observations secured in 2006 by Petr Harmanec, Domagoj Ruždjak and Davor Sudar, and 4 observations secured during one night in 2024 by Hrvoje Božić. We use the mean values of all 25 observations, $U = 0.479 \pm 0.025$, $B = 1.487 \pm 0.034$, and $V = 1.679 \pm 0.018$. The SED data were calculated using the wavelengths from Bessell (2000) and calibration fluxes from Wilson et al. (2010). The resulting values of SED are in Table C.1.

2.4. Parallax

As ϵ Ori is too bright, it saturates Gaia’s detector, designed primarily for stars fainter than $G = 6$ mag, and its parallax measurements are not reliable. Hipparcos parallaxes were less precise; Perryman et al. (1997) estimated the distance of 412 pc, while van Leeuwen (2007) 606 pc. Instead, in Oplištilová et al. (2023), we used Gaia DR3 parallaxes of the faint stars in the same stellar association (Orion OB1b). We assumed that the most massive stars are located close to the median distance. Then the distance of ϵ Ori should be close to $d \approx 384$ pc, which is just intermediate between the other Orion Belt stars, ζ Ori (386 pc) and δ Ori (381 pc).

As a verification, we checked diffuse interstellar bands (DIBs). Their strength depends on the interstellar medium, not on a spectral type, and is correlated with the colour excess E_{B-V} , which quantifies the amount of dust/reddening along the line of sight (Friedman et al. 2011). We assumed that the interstellar medium in the direction of ϵ Ori has similar properties to other stars close on the sky. We used the same methodology as Guinan et al. (2012); we selected two stars (Table 2) that are not in a dusty region according to the WISE map (Baumann et al.

2022) and have both Gaia parallaxes and high-resolution spectra in public archives. Then, we compared the strengths of their DIBs (Fig. 1). The star HD 37140 shows significant DIBs at the distance of (420 ± 9) pc, while HD 36628 shows no DIBs at (242 ± 2) pc. Thus, we verified that ϵ Ori is likely located at the distance < 420 pc, and our previous estimate seems to be reasonable.

Similarly, the colour excess E_{B-V} is closely related to the distance. We thus computed E_{B-V} according to Johnson & Morgan (1953), using U , B , and V magnitudes from Blanco et al. (1970) and Mermilliod (1994), see Table 2. The colour excess of ϵ Ori is computed in Sect. 2.3. Moreover, according to Green et al. (2019)², there is a sudden ‘jump’ in reddening in this direction, occurring at a distance of 400 pc.

We conclude that the previous distance estimate of about 600 pc is certainly incorrect. The relation of E_{B-V} , the strengths of DIBs, and distance of ϵ Ori corresponds to our estimate, (384 ± 8) pc.

Table 2. Distances and reddening of stars, which are close to ϵ Ori on the sky. The corresponding DIBs observations are shown in Fig. 1.

Star	d [pc]	E_{B-V} [mag]	Spectral type
HD 37140	420 ± 9	0.256	B8 II*
ϵ Ori	384 (assumed)	0.050	B0 Ia
HD 36628	242 ± 2	0.030	B9 IV/V*

Notes. * Houk & Swift (1999)

3. ϵ Ori as a single star

We constructed a single-star model of the B0 Ia supergiant ϵ Ori using PHOEBE2³ (Prša et al. 2016; Horvat et al. 2018; Jones et al. 2020; Conroy et al. 2020). PHOEBE2 employs seamless triangular meshes, closely following the generalised Roche potential. Each triangular element of the mesh is assigned local quantities (e.g. temperature, surface gravity, intensity, directional cosine). The total flux is then computed by integrating over visible elements. PHOEBE2 incorporates various stellar atmosphere models, which enables a realistic, self-consistent treatment of limb darkening, gravity darkening, as well as rotational

² <http://argonaut.skymaps.info/>

³ <http://phoebe-project.org>

Table 3. Grid of almost spherical models for ε Ori assuming a fixed value of $v \sin i = 70 \text{ km s}^{-1}$. Except for the temperature T , all the parameters were determined from interferometry. The values of χ^2_{VIS} do not exhibit a significant minimum, because the model is too constrained by $v \sin i$. Then, we kept the determined parameters fixed and fitted the temperature according to the spectroscopic data to find χ^2_{SPE} . However, synthetic line profiles were in all cases deeper than the observed ones. The model with the lowest χ^2_{VIS} and χ^2_{SPE} is in bold.

i [deg]	m [M_{\odot}]	Ω [deg]	R_{equiv} [R_{\odot}]	θ_{equiv} [mas]	P_{rot} [d]	v [km s^{-1}]	$v \sin i$ [km s^{-1}]	χ^2_{VIS} [1]	T [K]	χ^2_{SPE} [10^3]
14	22.90	289.7	24.68	0.598	4.31	289	70	11.451	25384	13.4
15	23.99	289.9	25.26	0.612	4.72	270	70	11.532	25363	14.7
20	26.06	289.9	26.32	0.638	6.51	205	70	11.658	26366	17.0
30	27.12	290.5	26.85	0.650	9.70	140	70	11.715	26718	18.5
40	27.43	299.4	27.00	0.654	12.55	109	70	11.732	26929	18.9
50	27.58	290.2	27.08	0.656	14.99	91	70	11.740	27962	20.1
60	27.66	299.1	27.12	0.657	16.97	81	70	11.743	27956	20.3
70	27.68	290.5	27.13	0.657	18.43	74	70	11.745	27198	19.3
80	27.68	290.1	27.13	0.657	19.31	71	70	11.747	28041	20.4
90	27.71	290.0	27.14	0.657	19.62	70	70	11.746	28050	20.4

Notes. i denotes the inclination of the spin axis with respect to the sky plane; m , mass; Ω , the orientation of star's equator, as seen by the observer; R_{equiv} , equivalent radius; θ_{equiv} , angular diameter; P_{rot} , rotational period; v , circumference velocity. For models based on interferometry, the parameters i , $\log g = 3.0$, $v \sin i = 70 \text{ km s}^{-1}$, $T = 25000 \text{ K}$ were fixed, while m , Ω were free.

Table 4. Grid of non-spherical models of ε Ori without a $v \sin i$ constraint. Otherwise, χ^2_{VIS} and χ^2_{SPE} were computed as in Table 3. The best-fit model based on interferometry is shown in Fig. 6, while the one based on spectroscopy is in Fig. 7.

i [deg]	m [M_{\odot}]	Ω [deg]	R_{equiv} [R_{\odot}]	θ_{equiv} [mas]	P_{rot} [d]	v [km s^{-1}]	$v \sin i$ [km s^{-1}]	χ^2_{VIS} [1]	T [K]	χ^2_{SPE} [10^3]
0	23.75	306.1	25.20	0.610	4.85	None	0	12.188	25300	71.7
10	23.87	307.2	25.26	0.612	4.80	266	46	11.949	25283	31.7
20	21.47	290.2	23.96	0.580	3.99	304	104	10.273	24537	1.9
30	23.46	300.6	25.04	0.607	4.07	311	155	8.734	23970	15.4
40	24.96	308.1	25.83	0.626	4.14	316	203	7.363	23378	43.0
50	26.73	300.8	26.73	0.648	4.21	321	246	6.959	22747	68.1
60	28.18	301.3	27.45	0.665	4.27	325	282	6.929	22282	85.8
70	28.58	300.7	27.64	0.669	4.28	326	307	6.967	21997	96.1
80	28.27	298.6	27.49	0.666	4.36	319	314	7.222	22018	100.0
90	28.16	298.1	27.44	0.665	4.44	312	312	7.339	22192	100.0

Notes. The parameters i (range of value), $\log g = 3.011$, and $T = 24985$ were fixed, while m , Ω , P_{rot} free.

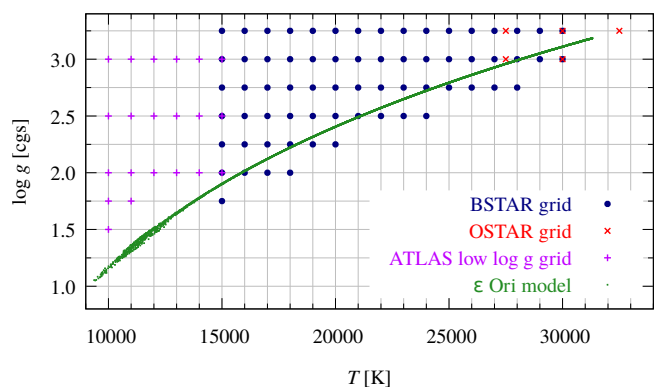


Fig. 4. Grids of synthetic spectra BSTAR and OSTAR (Lanz & Hubeny 2003; Lanz & Hubeny 2007), used in our spectroscopic models. Each spectrum is parametrised by $\log g$ and T . In order to describe also critically rotating stars (cf. green points), it was necessary to compute additional ATLAS spectra (Castelli & Kurucz 2003) for low values of $\log g$ and T .

distortion. It is a powerful tool for solving an inverse problem, constrained by light curves and radial velocity curves, and re-

cently, it was extended to include interferometry, spectra, and SED.

A new interferometric module of PHOEBE2⁴ (Brož et al. 2025b) enables computations of interferometric observables—squared visibility (V^2), closure phase ($\arg T_3$), and amplitude ($|T_3|$)—by means of the Fourier transform approach. Additionally, a new spectroscopic module (Brož et al. 2025a) utilises interpolations in grids of synthetic spectra, assigning one spectrum to each element. Again, the total spectrum is obtained by integrating over all elements, weighted by appropriate passband intensities. It allows fitting of detailed spectral line profiles.

Visibility. First, we modelled ε Ori as a spherical star with fixed radiative parameters according to Puebla et al. (2016a), namely, $T = (27000 \pm 500) \text{ K}$ and $\log g = (3.00 \pm 0.05)$ that they estimated by the fitting of line profiles of H_{β} , H_{γ} , H_{δ} , H_{ϵ} . In PHOEBE2, we set the Kurucz atmospheres, but linear limb darkening coefficient $c_1 = 0.01621$ interpolated from van Hamme (1993) tables for comparison purposes (see below). We assumed the distance $d \approx 384 \text{ pc}$, as discussed in Sect. 2.4. We verified the computation of V^2 using the independent implementation of Brož (2017). The fitting of V^2 using the implementation of PIONIER and the convergence of one

⁴ <https://github.com/miroslavbroz/phoebe2>

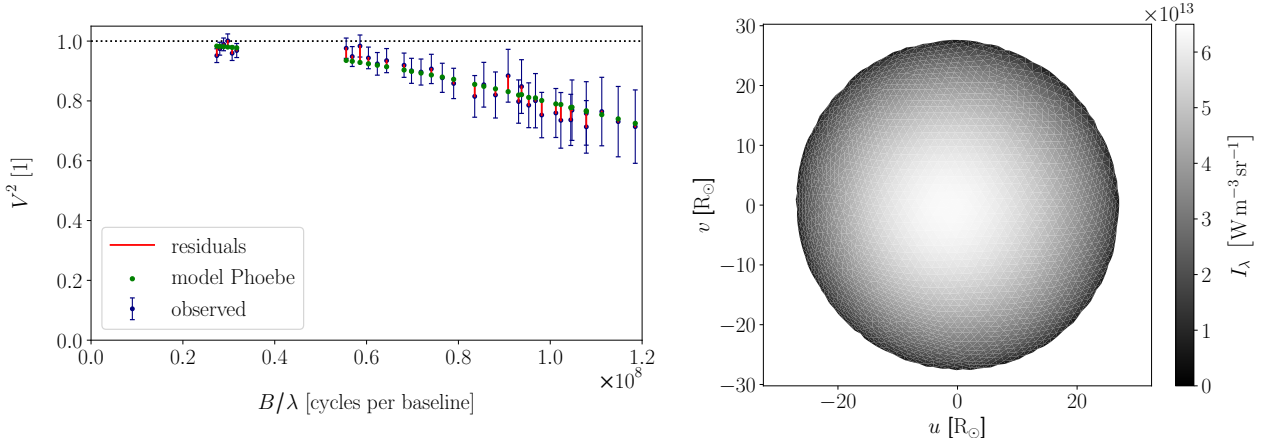


Fig. 5. Almost spherical model of ϵ Ori based on PIONIER observations in passband Johnson:H. Left: squared visibility vs. projected baseline B/λ ; right: corresponding triangular mesh with the passband intensities (grayscale). fixed $v \sin i$ (Puebla et al. 2016b). The model was converged starting with the parameters from Table 3 (bold line). The best-fit was with $\chi^2_{\text{VIS}} = 11.23$. The free parameters were $i = 13.6$ deg, $m = 20.3 M_{\odot}$, $\Omega = 293.7$ deg, $P_{\text{rot}} = 4.01$ d; the fixed parameters, $v \sin i = 70 \text{ km s}^{-1}$, $T = 25\,000 \text{ K}$, $\gamma = 25.9 \text{ km s}^{-1}$; and the derived parameters, $v = 298 \text{ km s}^{-1}$, $R_{\text{equiv}} = 22.43 R_{\odot}$ (derived), $R_{\text{pole}} = 22.29 R_{\odot}$ (derived), $R_{\text{equ}} = 22.46 R_{\odot}$ (derived), $\theta_{\text{equiv}} = 0.543$ mas. The star is close to critical rotation and has almost pole-on orientation in order to decrease projected rotation (cf. $v \sin i$).

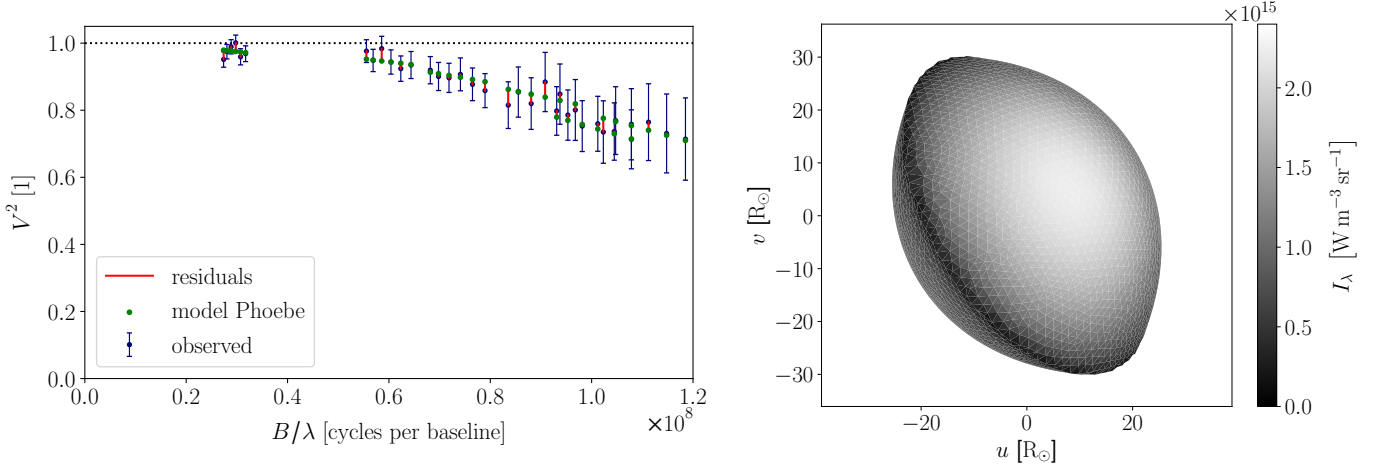


Fig. 6. The same as Fig. 5, but with free $v \sin i$. The model was converged starting with the parameters from Table 4. The best fit model was with $\chi^2_{\text{VIS}} = 6.928$. The free parameters were $i = 58.3^{\circ}$, $m = 28.0 M_{\odot}$, $\Omega = 301.5$ deg, $P_{\text{rot}} = 4.26$ d; the fixed parameters, $T = 27\,000 \text{ K}$, $\gamma = 25.9 \text{ km s}^{-1}$; and the derived parameters, $v \sin i = 277 \text{ km s}^{-1}$, $v = 325 \text{ km s}^{-1}$, $R_{\text{equiv}} = 27.37 R_{\odot}$, $R_{\text{pole}} = 22.29 R_{\odot}$, $R_{\text{equ}} = 33.61 R_{\odot}$, $\theta_{\text{equiv}} = 0.667$ mas, $\theta_{\text{pole}} = 0.540$ mas, and $\theta_{\text{equ}} = 0.814$ mas. Again, the star is close to the critical rotation, but with an oblique orientation. This model better explains the visibilities along different baselines B/λ . The meaning of Ω is illustrated.

free parameter (m) using the simplex method (Nelder & Mead 1965) resulted in exactly the same $\chi^2_{\text{VIS}} = 12.1$ in both codes (Fig. D.3). The χ^2 value is smaller than the number of degrees of freedom $\nu = N - M = 35$, which most likely indicates over-estimated uncertainties of PIONIER observations. In fact, previous PIONIER observations were more precise (Pietrzyński et al. 2019). If the uncertainties are properly rescaled, the best-fit mass is $m = (23.5 \pm 0.5) M_{\odot}$, corresponding to the angular diameter $\theta = (0.615 \pm 0.007)$ mas and physical radius $R = (25.4 \pm 0.3) R_{\odot}$.

Second, we modelled a rotating, almost spherical star. For simplicity, we used black-body atmospheres to avoid problems with too low $\log g$ values, occurring when the star is close to the critical rotation (cf. Fig. 4). Nevertheless, we derived the limb darkening coefficients from the Kurucz atmospheres and set them manually, with a power-law prescription (Prša et al. 2016)

$$\frac{I}{I_0} = 1 - c_1(1 - \mu^{\frac{1}{2}}) - c_2(1 - \mu) - c_3(1 - \mu^{\frac{3}{2}}) - c_4(1 - \mu^2), \quad (4)$$

where $c_1 = 1.698$, $c_2 = -4.151$, $c_3 = 5.887$, $c_4 = -2.525$ are suitable for the temperature $T = 27\,000 \text{ K}$ and $\log g = 3.0$ (Puebla et al. 2016a). We set the bolometric gravity brightening exponent $\beta = 1.0$, which corresponds to hot stars ($T > 8000 \text{ K}$), assuming that the local temperature is proportional to

$$T = T_{\text{pole}} (g/g_{\text{pole}})^{0.25\beta}, \quad (5)$$

where g is the local gravitational acceleration. To reveal all possible minima of χ^2 , we computed a more detailed grid in inclination of the rotation axis (hereafter only ‘inclination’) i . The orientation of the star is also determined by Ω , longitude of the ascending node (of the equator). We made the parameters m and Ω free, the parameters $\log g$, d , $v \sin i$ (and i) fixed, while the dependent parameters P_{rot} , R_{equiv} , θ_{equiv} were constrained by the following relations

$$P_{\text{rot}} = \frac{2\pi R_{\text{equiv}}}{v \sin i} \sin i, \quad (6)$$

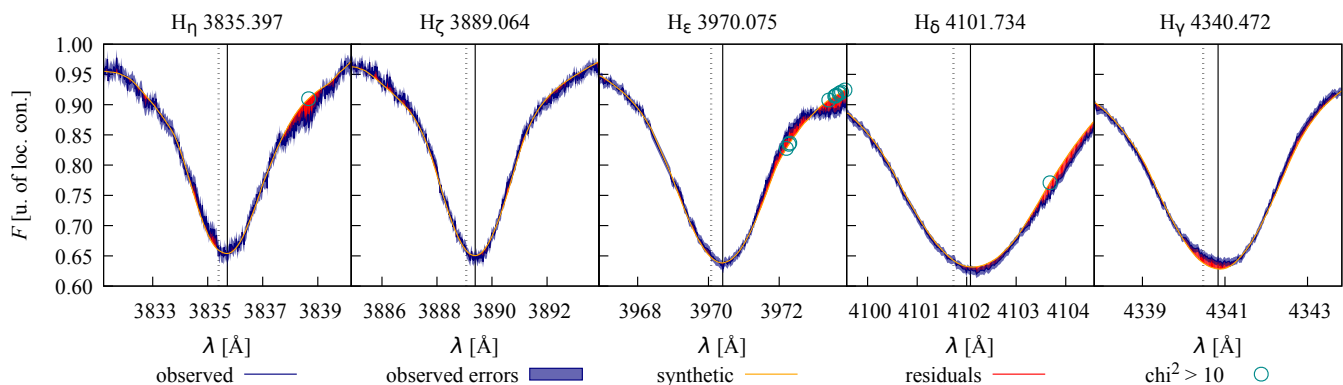


Fig. 7. Almost spherical model of ϵ Ori based on CFHT spectroscopy. Hydrogen Balmer lines were fitted using 1443 data points, excluding H_α and H_β , which are ‘filled’ by wind-induced emission. An interstellar calcium 3968 Å for H_ϵ was masked. The best fit resulted in $\chi^2_{\text{SPE}} = 1770$. Free parameters were $P_{\text{rot}} = 4.551$ d, $T = 25037$ K, $\log g = 3.016$, $i = 21.40$ deg, and $\gamma = 25.00$ km s $^{-1}$. Other parameters were fixed and set according to interferometry. The derived parameters were $v \sin i = 111$ km s $^{-1}$ and $v = 305$ km s $^{-1}$. The dotted lines show laboratory wavelengths, while the solid vertical lines indicate the Doppler-shifted line centres, corresponding to the resulting γ . The teal circles denote the points that contributed to χ^2 with values greater than 10. This model explains reasonably well the Balmer lines, with a few systematics remaining in H_ϵ , H_η , possibly due to different metal abundances. The temperature was constrained, and $\log g$ was slightly adjusted. However, due to the difference in inclination ($i = 21$ vs. 62 deg), the interferometric model would become worse, with $\chi^2_{\text{VIS}} = 16.04$.

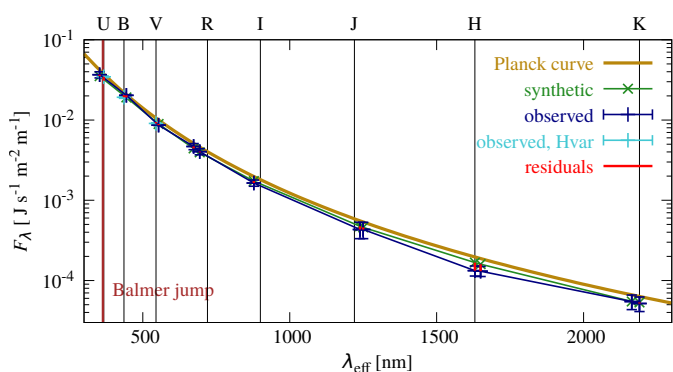


Fig. 8. SED model of ϵ Ori based on data from the Hvar Observatory and Vizier—the monochromatic flux F_λ vs. wavelength λ . The best-fit value was $\chi^2_{\text{SED}} = 52$ with the following parameters: $T_{\text{eff}} = 24654$ K (fitted), $d = 384$ pc (fixed), $M = 28.43 M_\odot$ (fixed), $R = 27.45 R_\odot$ (derived); other parameters were fixed and set according to interferometry. This model served as an independent verification of the temperature from the spectroscopic model.

$$R_{\text{equiv}} = \sqrt{\frac{Gm}{g}}, \quad (7)$$

$$\theta_{\text{equiv}} = \frac{2R_{\text{equiv}}}{d}, \quad (8)$$

where the value of $v \sin i$ was set up to 70 km s $^{-1}$ (Puebla et al. 2016a).

The converged models for fixed values of i are listed in Table 3. Unfortunately, the models were too constrained by the fixed value of $v \sin i$; the χ^2_{VIS} dependence on i remained flat over the full range of i . Formally, the lowest χ^2_{VIS} value is for the lowest inclination, $i = 14$ deg. Lower values of i cause problems in modelling of edges. For the best-fit model, converged from parameters with the lowest χ^2_{VIS} , see Fig. 5. It is a almost spherical star close to critical rotation, with almost pole-on orientation.

To obtain a model that best corresponds to the measured squared visibilities, we relaxed the $v \sin i$ constraint and computed another grid in i , using still only the interferometric data. In this case, there were three free parameters, m , Ω , and P_{rot} . Our results are summarised in Tab. 4. Fortunately, χ^2_{VIS} substantially decreased, from 12.2 down to 6.9, and the best-fit model is again a critically rotating star, seen at an oblique inclination of $i = (58 \pm 20)$ deg (see Fig. 6). On the other hand, the nominal projected velocity, $v \sin i = 277^{+30}_{-80}$ km s $^{-1}$, seems to be too high.

Spectroscopy. To constrain radiative parameters, which were only assumed in the previous interferometric models, we used the spectra from CFHT. First, we checked the influence of i , i.e. $v \sin i$, on synthetic line profiles, by computing forward models for the Balmer lines, H_γ , H_δ , H_ϵ , H_ζ , H_η , that are not much influenced by the wind (Puebla et al. 2016a). We used narrow ranges of wavelengths (± 3 , ± 2.5 , ± 4 , ± 5 , ± 5) Å, respectively, in order to eliminate neighbouring lines. Also, we masked one remaining interstellar calcium line 3968 Å near H_ϵ . In PHOEBE2, we set `spe_method` to ‘integrate’ and set the interpolation to nearest-neighbour, to remain within the respective grid (Fig. 4) and prevent excessive extrapolation. Furthermore, we computed additional ATLAS synthetic spectra (Castelli & Kurucz 2003)⁵ for low values of $\log g$ and T , to describe critically rotating stars.

The resulting χ^2_{SPE} values for fixed $v \sin i$ are listed in Table 3 and for relaxed $v \sin i$, in Table 4. The χ^2_{SPE} contribution to the total χ^2 is more than 3 orders of magnitude larger than χ^2_{VIS} because of the number of measurements. While χ^2_{SPE} and χ^2_{VIS} are the lowest for $i = 14$ deg in the models with fixed $v \sin i$, there is a tension between spectra and visibilities for models with relaxed $v \sin i$, which describes the interferometric data much better.

For comparison, we reconverged a model based only on spectroscopy, starting from the parameters with the lowest χ^2_{SPE} in Tab. 4 (bold); again with relaxed $v \sin i$. The best-fit model is shown in Fig. 7, corresponding to $\chi^2_{\text{SPE}} = 1797$. The free parameters and their resulting values were $P_{\text{rot}} = 4.535$ d, $T = 24915$ K, $\log g = 3.01$, $i = 21.0$ deg. Other parameters were fixed and set according to interferometry. The derived projected velocity,

⁵ <https://github.com/RozanskiT/vidmapy>

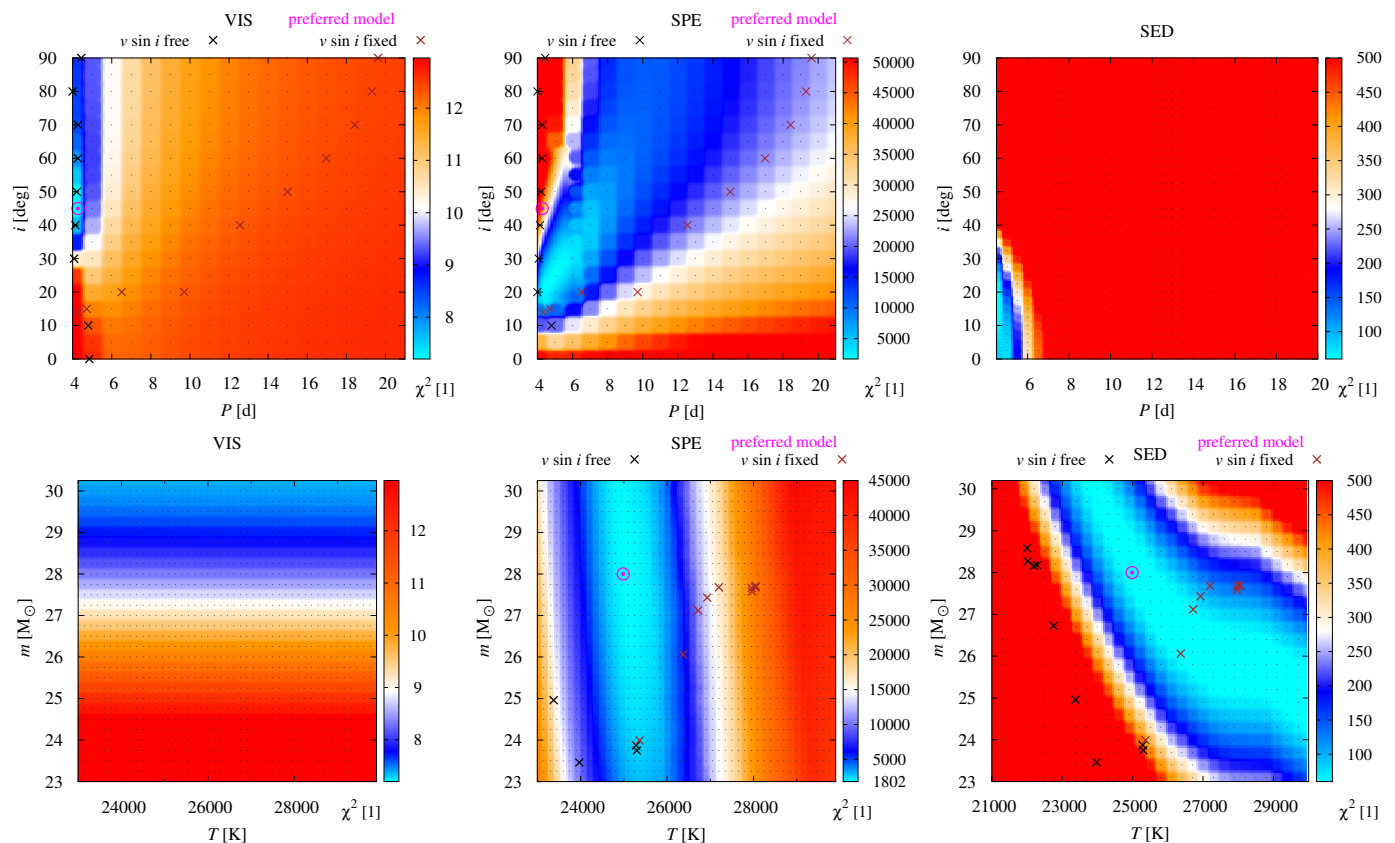


Fig. 9. Maps of χ^2 for the ϵ Ori model. We performed 2D mapping of χ^2 across different datasets: squared visibilities (VIS), spectral lines of Balmer series (SPE), and spectral energy distribution (SED). We systematically varied two parameters to create a regular grid (P_{rot} vs. i in the first row, T vs. m in the second row). The remaining parameters were held fixed. The colour scale was adjusted as follows: cyan—the best fit for a given data set, blue—acceptable fits, white—poor fits, orange—unacceptable fits, red—forbidden regions. In the first row, the fixed parameters are those resulting from the best fit of interferometric data in Fig. 6: d , m , and Ω ; other fixed parameters are $T = 25\,000$ K, $\log g = 3.011$, and $\gamma = 25.9$ km s $^{-1}$. The dependent parameters were R_{equiv} and $v \sin i$. In the second row, we set P_{rot} and i according to the best fit in the first row. The individual panels, from the upper left, are as follows: I) VIS dataset shows a preference for a critically rotating star and i around 45 deg. II) SPE dataset (H lines) shows a preference for a fast-rotating star, $P_{\text{rot}} = 5$ d, $i = 25$ deg. The correlation between P_{rot} and i is due to rotation and $v \sin i$. III) SED dataset also allows a critically or fast-rotating star for i close to 20 deg. However, it is possible to re-fit T , R , or d to achieve improved SED fits in other regions of the parameter space. IV) VIS dataset shows a flat dependence on temperature and the preferred mass. V) SPE dataset for H lines demonstrates a weak correlation between T and m , the best-fit of T is around 25 000 K. VI) SED dataset is strongly correlated between T and m due to the Stefan–Boltzmann law and Eq. (7). The crosses mark the models from Tables 3 and 4.

$v \sin i = 111$ km s $^{-1}$, is substantially lower. A forward model based on parameters from interferometry, with higher $v \sin i$, gives smeared lines, while the observed lines are sharper.

Closure phase. Unfortunately, even though closure phases are very useful to detect photocentre offsets, the observed amplitude from PIONIER seems to be too high (up to 4 deg) compared to any of our models. Even critically rotating stars, which have the largest differences of polar-to-equatorial temperatures, exhibit synthetic amplitudes less than 0.1 deg (Fig. D.4). Nevertheless, taking into account only the signs and trends of $\arg T_3$ vs. λ , synthetic closure phases should change in the same sense as observed ones, which allowed us to resolve the Ω ambiguity (120 vs. 300 deg) in Sect. 3.

SED. As an independent check, we computed the PHOEBE2 model for the SED (using again the new module). As synthetic spectra, we used the absolute fluxes from the BSTAR, OSTAR, and ATLAS grids. The observed SED values were dis-

cussed in Sect. 2.3. We converged only the effective temperature T_{eff} . Other parameters were fixed according to the model based on interferometry (from Fig. 6). The resulting value was $T_{\text{eff}} = 24\,880$ K, which is very close to the value inferred from the fitting of Balmer lines. Our model was in good agreement with the observed SED; see Fig. 8.

Compromise model. Finally, we computed two-dimensional χ^2 maps to better understand mutual relations between datasets (see Fig. 9). We always distinguished individual contributions to χ^2 , namely from interferometry (VIS), spectroscopy (SPE) and SED (SED). In each panel, we were changing only two parameters to get a regular grid, while others parameters are kept fixed. For mapping, we chose the period P_{rot} from 4 d to 20 d with the step of 0.5 d vs. the inclination i from 0 deg to 90 deg with the step of 5 deg. Alternatively, we chose the temperature T from 21 000 K to 30 000 K with the step of 500 K vs. the mass m from 21 M_{\odot} to 32 M_{\odot} with the step of 0.5 M_{\odot} . Let us recall that m is always related to R_{equiv} (Eq. (7)).

The VIS maps with squared visibility measurements show a preference for a critically rotating, oblate star, seen at an oblique angle (40 to 60 deg). On the other hand, there is a negligible dependence on temperature. A higher mass (28 to 30 M_{\odot}) is preferred, but this is certainly correlated with the distance (Eq. (8)).

The SPE maps with Balmer lines demonstrate that only lower inclinations can appropriately fit the depth and width of spectral lines. There is a weak correlation between the mass and temperature, indicating the appropriate temperature is around 25 000 K and not well-constrained mass.

The SPE maps based on He I lines (Fig. 10) is quite similar. Although there is a correlation of good fits between i and P_{rot} , we see a possible solution for a fast-rotating star, with a similar inclination to that derived from the Balmer lines. Again, the mass and temperature are weakly correlated, indicating the temperature 25 000 K. (The fits around 28 000 K resulted in poorer line depths.)

The SED maps are, of course, strongly influenced by the fixed temperature and mass, but show good solutions for a critically rotating star, with a similar inclination as for spectra. The mass and temperature are strongly correlated.

We conclude that the inclination is the only uncertain parameter, for which the results differ according to interferometry (40 to 60 deg) vs. spectroscopy (10 to 30 deg). Other parameters correspond to all three kinds of observations. As a compromise, we prefer the value around 40 deg, which partly explains both the interferometry and the spectroscopy. The resulting parameters of ε Ori are summarised in Table 5.

4. Discussion

Our interferometry of ε Ori can be compared to [Abeysekara et al. \(2020\)](#), who acquired intensity interferometry in B band. Their limb-darkened angular diameter, $\theta_{\text{LD}} = (0.660 \pm 0.018)$ mas, is in perfect agreement with our measurements in H band (Tab. 5).

However, as discussed in Sect. 3, the observed closure phases are high (up to 4 deg) compared to our model. This raises the question: what could be missing in our model?

Possible binarity. Such a modest amplitude in closure phases indicates a flux asymmetry with low contrast, up to $4^{\circ} = 0.07$ rad = 7%, in the Johnson:H passband. For this estimate, we assumed a maximally asymmetric object (i.e. a binary) and used the following closure phase approximation, $\arg T_3 \approx F_2/F_1 \sin(2\pi \frac{B\phi}{\lambda})$, where F_1 , F_2 denote the fluxes of the two stars and ϕ the angular scale. Based on this, we estimated the mass of the companion, assuming that it is on the main sequence, to $\sim 12 M_{\odot}$. To explain the observed dependence on B/λ , the angular scale should be of the order of 0.5 mas, corresponding to $\sim 40 R_{\odot}$. From this, we estimated the orbital period, $P = 2\pi \sqrt{a^3/(GM)} \approx 6$ d, assuming the total mass $\sim 30 M_{\odot}$, i.e. of the same order as the primary. RV amplitudes for the primary and secondary are of the order of a hundred km s^{-1} , but these could be suppressed by orbit orientation (e.g. for $i = 5^{\circ}$, 15 km s^{-1}). In the dataset of [Thompson & Morrison \(2013\)](#), there are RV variations of this order observed in the He I 5876 Å line. However, they are not persistent, and they cannot be phased with a fixed period. Only for one season, [Thompson & Morrison \(2013\)](#) reported a period of about 5 d. In the context of our model, this could correspond to the rotation period of the primary, or even more likely, to the variability of circumstellar material.

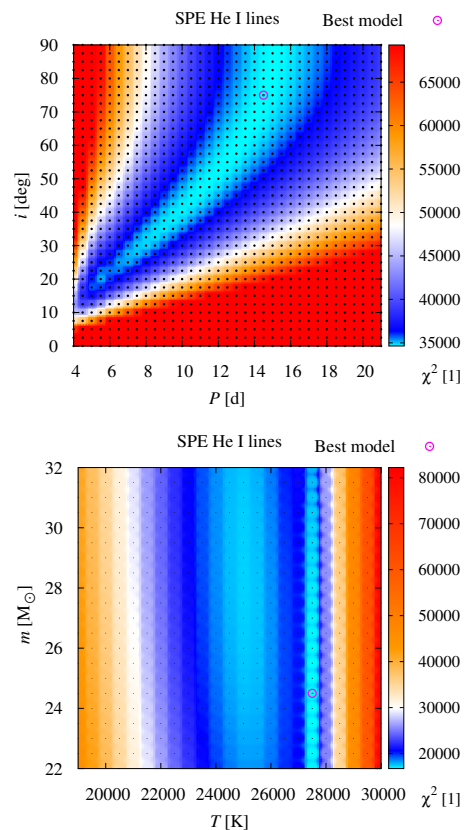


Fig. 10. The same as Fig. 9, but for the spectroscopic dataset based on He I lines. Top: SED dataset for He I lines exhibits results very similar to spectroscopy based on Balmer lines. The higher P_{rot} and i values are excluded because of other datasets. Bottom: SED dataset for He I lines, indicating two possible solutions at $T = 25$ 000 K or 27 500 K due to systematic offsets in some lines. The model with $T = 25$ 000 K fits better the depths of He I lines. The map also shows no preference for the mass.

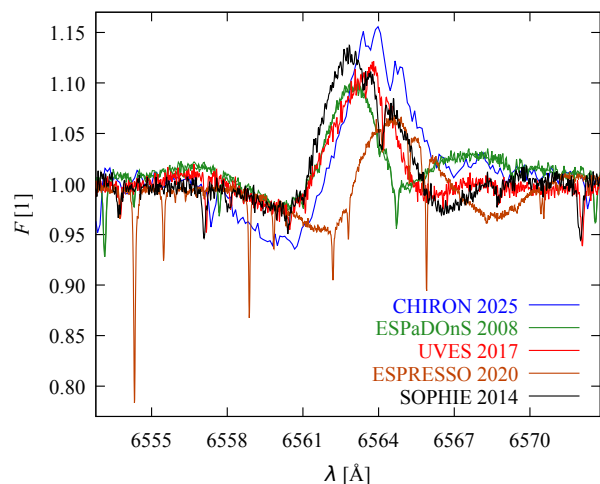


Fig. 11. Spectroscopy of ε Ori showing the H_{α} line profile that is highly variable and can be in several morphologies, like P Cygni profile, inverse P Cygni profile, double emission, or pure emission ([Thompson & Morrison 2013](#)). It implies an intense wind (e.g. [Puebla et al. 2016b](#)), or a decretion disk fed by mass loss from the star. This variable line was not used in our modelling.

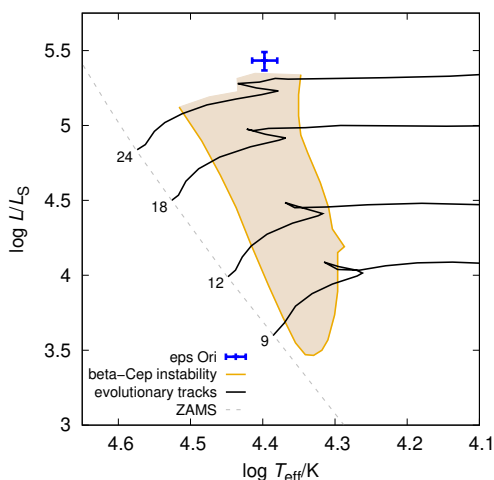


Fig. 12. Hertzsprung–Russell diagram showing the position of ϵ Ori (blue) in comparison to the β -Cep instability region ($\ell = 0$; orange) and several evolutionary tracks (black) from Paxton et al. (2015). Note that the instability was computed only up to $24 M_{\odot}$, but the region most likely continues upwards, and the instability also occurs for the luminosity class Ia ($\log L/L_{\odot} \geq 5.3$).

Table 5. Resulting parameters of ϵ Ori based on a compromise among interferometry, spectroscopy, and SED.

Parameter	Value	Uncertainty	Unit	Note
m	28.42	2.0	M_{\odot}	fitted
P_{rot}	4.27	$^{+1.0}_{-0.0}$	d	fitted
i	45	20	deg	fitted
Ω	301.6	30	deg	fitted
d	384	8	pc	fixed
T_{eff}	24985	1000	K	fixed
$\log g$	3.011	0.1	cgs	fixed
β	1.0	0.1	1	fixed
γ	25.0	0.9	km s^{-1}	derived
γ_{LSR}	8.2	0.7	km s^{-1}	derived
R_{equiv}	27.36	1.5	R_{\odot}	derived
R_{pole}	22.29	1.2	R_{\odot}	derived
R_{equ}	33.61	1.8	R_{\odot}	derived
θ_{equiv}	0.667	0.035	mas	derived
θ_{pole}	0.540	0.064	mas	derived
θ_{equ}	0.814	0.073	mas	derived
L	271 000	38 000	L_{\odot}	derived
$v \sin i$	220	$^{+40}_{-100}$	km s^{-1}	derived
v	326	$^{+50}_{-120}$	km s^{-1}	derived
f	1.47	0.35	rad/d	derived

Notes. m denotes the mass; P_{rot} , the rotation period; i , the inclination of the stellar rotation axis with respect to the sky; Ω , the longitude of the ascending node of the star (i.e. equator); d , the distance; T_{eff} , the effective temperature; $\log g$, the logarithm of surface gravity; β , bolometric gravity brightening exponent; γ , the systemic velocity; γ_{LSR} , the systemic velocity with respect to the local standard of rest; R_{equiv} , the equivalent radius; R_{pole} , the pole radius; R_{equ} , the equatorial radius; θ_{equiv} , the equivalent angular diameter; θ_{pole} , the polar angular diameter; θ_{equ} , the equatorial angular diameter; L , the luminosity; $v_{\text{rot}} \sin i$, the projected rotation velocity; v_{rot} , the rotation velocity; and f , the rotation frequency.

Wind. Another asymmetry could be related to wind (Puebla et al. 2016b), if the material expelled from ϵ Ori is not evenly distributed, but concentrated in relatively dense clumps. This phenomenon is especially relevant for hot, massive stars like B supergiants, O-type stars, or Wolf-Rayet stars (Puls et al. 2008; Krtićka et al. 2021). Only if clumps are locally optically thick in the Johnson:H passband, they contribute to the respective continuum flux and the closure phase signal observed by PIONIER. Otherwise, wind is observed in H_{α} line (Fig. 11), which is highly variable and exhibits a range of morphologies, from a classical P Cygni profile, an inverse P Cygni profile, double emission, to pure emission (see also Thompson & Morrison 2013, Fig. 1).

Disk. An additional asymmetry might be produced by an unresolved disk, fed by mass loss from the star, and partially eclipsed by the star. If this is the source of the double emission sometimes observed in the wings of H_{α} (Fig. 11), the redshift and the blueshift, $\Delta\lambda \simeq 6 \text{ \AA}$, are interpreted as rotation, $\Delta v = \Delta\lambda/\lambda c = 274 \text{ km s}^{-1}$. This is surprisingly similar to the projected velocity $v \sin i$ in our models of ϵ Ori. Finally, if the star is close to critical rotation, as indicated by the PIONIER observations, we naturally expect an ongoing outflow from the equator.

Pulsations. Moreover, ϵ Ori is close to the β Cep instability region (Paxton et al. 2015) for low-order modes $\ell = 0, 1, 2$ (see Fig. 12). Photometric observations of ϵ Ori seem to be compatible with typical periods ranging from 0.1 to 0.6 d, and the amplitudes ~ 0.1 mag for β Cep variables (Lesh & Aizenman 1978). Such pulsations can enhance mass loss, especially if the star is rotating near its critical velocity. On the other hand, the periodograms for BRITTE light curves or for RVs do not exhibit distinct peaks Krtićka & Feldmeier (2018); Thompson & Morrison (2013), so their interpretation is stochastic, episodic activity due to mass loss.

Stellar evolution. If we—for the moment—assume a standard stellar evolution model for a $28.4 M_{\odot}$, rotating star, it takes ~ 7.3 My to evolve from the zero-age main sequence to B0Ia (Ekström et al. 2012; Paxton et al. 2013). This is about 25% longer than for a non-rotating star due to enhanced mixing and homogenised composition. For comparison, there are two groups of low-mass, young stellar objects (YSOs) observed in the vicinity of ϵ Ori, denoted ‘Orion C’ and ‘Orion D’ (Kounkel et al. 2018). Their ages span from approximately 0.3 to 5.5 My. They were classified as Class II or III, as some are still accreting and associated with translucent gas clouds (Briceño et al. 2005). This implies either that the stellar evolution for ϵ Ori was non-standard, e.g. with extreme mass loss, or the formation of low- and high-mass stars was not *eodem loco et tempore*. Additionally, both the distance and the systemic velocity of ϵ Ori (384 pc and 8 km s^{-1} ; measured with respect to the local standard of rest) seem to be in the middle, between Orion C and Orion D groups (Kounkel et al. 2018, Fig. 11). This relation might suggest that high-mass stars form either a bit earlier than low-mass stars or elsewhere (Sanhueza et al. 2017; Maud et al. 2018).

5. Conclusions

We obtained and calibrated VLTI/GRAVITY and PIONIER interferometric data for the brightest stars in the Orion Belt, the closest star-forming region. In this first paper, we modelled the supergiant ϵ Ori based on VLTI/PIONIER visibility data, CFHT and CTIO spectra, and absolute fluxes. While the models based on interferometry indicate an oblate, critically rotating star, the models based on spectroscopy indicate a fast-rotating, less oblate star. The fast rotation might imply that ϵ Ori is a merger.

We also discussed the possibility of binarity, based on the asymmetry visible in closure phase data. However, due to the lack of consistent radial velocity variations, we excluded this binary model. We rather attributed the asymmetry to the clumped stellar wind or possibly to a decretion disk. To better constrain its properties, it is necessary to observe ϵ Ori with a spectro-interferometer such as CHARA/SPICA (Mourard et al. 2024), which is capable of scanning across the H_α line.

In a forthcoming second paper, we will focus on the multiple stellar systems in the Orion Belt.

Acknowledgements. A.O. was supported by GA UK grant no. 113224 of the Grant Agency of Charles University. M.B. was supported by GA ČR grant no. 25-16507S of the Czech Science Foundation. We thank other observers at the Hvar Observatory, Hrvoje Božić, Domagoj Ruždjak, and Davor Sudar for securing data for ϵ Ori.

References

- Abbott, R., Abbott, T. D., Abraham, S., et al. 2021, *ApJ*, 913, L7
- Abeyskera, A. U., Benbow, W., Brill, A., et al. 2020, *Nature Astronomy*, 4, 1164
- Allen, M. G., Ochsenbein, F., Derriere, S., et al. 2014, in *Astronomical Society of the Pacific Conference Series*, Vol. 485, *Astronomical Data Analysis Software and Systems XXIII*, ed. N. Manset & P. Forshay, 219
- Almeida, L. A., Sana, H., de Mink, S. E., et al. 2015, *ApJ*, 812, 102
- Anderson, E. & Francis, C. 2012, *Astronomy Letters*, 38, 331
- Atri, P., Miller-Jones, J. C. A., Bahramian, A., et al. 2019, *MNRAS*, 489, 3116
- Baumann, M., Boch, T., Pineau, F.-X., et al. 2022, in *Astronomical Society of the Pacific Conference Series*, Vol. 532, *Astronomical Data Analysis Software and Systems XXX*, ed. J. E. Ruiz, F. Pierfederici, & P. Teuben, 7
- Bessell, M. 2000, in *Encyclopedia of Astronomy and Astrophysics*, ed. P. Murdin, 1939
- Blanco, M., Demers, S., & Douglass, G. G. 1970, *Photoelectric catalogue - Magnitudes and colors of stars in the U, B, V and U_c, B, V systems*
- Božić, H. & Harmanec, P. 2023, *Highlights of a half century of the UVB photometry at Hvar*
- Briceño, C., Calvet, N., Hernández, J., et al. 2005, *AJ*, 129, 907
- Brož, M. 2017, *ApJS*, 230, 19
- Brož, M., Prša, A., Conroy, K. E., & Abdul-Masih, M. 2025a, *A&A* in prep.; <https://arxiv.org/abs/2506.20868> [arXiv:2506.20868]
- Brož, M., Prša, A., Conroy, K. E., Oplištilová, A., & Horvat, M. 2025b, *A&A* in prep.; <https://arxiv.org/abs/2506.20865> [arXiv:2506.20865]
- Castelli, F. & Kurucz, R. L. 2003, in *IAU Symposium*, Vol. 210, *Modelling of Stellar Atmospheres*, ed. N. Piskunov, W. W. Weiss, & D. F. Gray, A20
- Clayton, D. D. 1983, *Principles of stellar evolution and nucleosynthesis*
- Conroy, K. E., Kochoska, A., Hey, D., et al. 2020, *ApJS*, 250, 34
- Corcoran, M. F., Nichols, J. S., Pablo, H., et al. 2015, *ApJ*, 809, 132
- Cutri, R. M., L., W. E., & Conrow, T. 2012, *VizieR Online Data Catalog*, II/311
- Cutri, R. M., Skrutskie, M. F., van Dyk, S., et al. 2003, *VizieR Online Data Catalog*, II/246
- Ducati, J. R. 2002, *VizieR Online Data Catalog*
- Egan, M. P., Price, S. D., Kraemer, K. E., et al. 2003, *VizieR Online Data Catalog*, V/114
- Eisenhauer, F., Perrin, G., Brandner, W., et al. 2011, *The Messenger*, 143, 16
- Ekström, S., Georgy, C., Eggenberger, P., et al. 2012, *A&A*, 537, A146
- Fan, H., Welty, D. E., York, D. G., et al. 2017, *ApJ*, 850, 194
- Freudling, W., Romaniello, M., Bramich, D. M., et al. 2013, *A&A*, 559, A96
- Friedman, S. D., York, D. G., McCall, B. J., et al. 2011, *ApJ*, 727, 33
- Gaia Collaboration. 2020, *VizieR Online Data Catalog*, I/350
- Gaia Collaboration, Brown, A. G. A., Vallenari, A., et al. 2021, *A&A*, 649, A1
- Golay, M. 1974, *Introduction to astronomical photometry*
- GRAVITY Collaboration, Abuter, R., Accardo, M., et al. 2017, *A&A*, 602, A94
- Green, G. M., Schlafly, E., Zucker, C., Speagle, J. S., & Finkbeiner, D. 2019, *ApJ*, 887, 93
- Guinan, E. F., Mayer, P., Harmanec, P., et al. 2012, *A&A*, 546, A123
- Hainich, R., Rühling, U., Todt, H., et al. 2014, *A&A*, 565, A27
- Horvat, M., Conroy, K. E., Pablo, H., et al. 2018, *ApJS*, 237, 8
- Houk, N. & Swift, C. 1999, *Michigan Spectral Survey*, 5, 0
- Hummel, C. A., Rivinius, T., Nieva, M. F., et al. 2013, *A&A*, 554, A52
- Hummel, C. A., White, N. M., Elias, N. M., I., Hajian, A. R., & Nordgren, T. E. 2000, *ApJ*, 540, L91
- Ishihara, D., Onaka, T., Kataza, H., et al. 2010, *A&A*, 514, A1
- Johnson, H. L. & Morgan, W. W. 1953, *ApJ*, 117, 313
- Jones, D., Conroy, K. E., Horvat, M., et al. 2020, *ApJS*, 247, 63
- Kalari, V. M., Horch, E. P., Salinas, R., et al. 2022, *ApJ*, 935, 162
- Keller, S. C., Schmidt, B. P., Bessell, M. S., et al. 2007, *PASA*, 24, 1
- Kounkel, M., Covey, K., Suárez, G., et al. 2018, *AJ*, 156, 84
- Krtićka, J. & Feldmeier, A. 2018, *A&A*, 617, A121
- Krtićka, J., Kubát, J., & Krtićková, I. 2021, *A&A*, 647, A28
- Lanz, T. & Hubeny, I. 2003, *ApJS*, 146, 417
- Lanz, T. & Hubeny, I. 2007, *ApJS*, 169, 83
- Le Bouquin, J. B., Berger, J. P., Lazareff, B., et al. 2011, *A&A*, 535, A67
- Lesh, J. R. & Aizenman, M. L. 1978, *ARA&A*, 16, 215
- Maíz Apellániz, J., Trigueros Páez, E., Negueruela, I., et al. 2019, *A&A*, 626, A20
- Marchant, P., Pappas, K. M. W., Gallegos-García, M., et al. 2021, *A&A*, 650, A107
- Maud, L. T., Cesaroni, R., Kumar, M. S. N., et al. 2018, *A&A*, 620, A31
- Mermilliod, J. C. 1994, *Bulletin d'Information du Centre de Données Stellaires*, 45, 3
- Mourard, D., Meilland, A., Ibañez Bustos, R., et al. 2024, in *Society of Photo-Optical Instrumentation Engineers (SPIE) Conference Series*, Vol. 13095, *Optical and Infrared Interferometry and Imaging IX*, ed. J. Kammerer, S. Sallum, & J. Sanchez-Bermudez, 1309503
- Nelder, J. A. & Mead, R. 1965, *The Computer Journal*, 7, 308
- Neugebauer, G., Habing, H. J., van Duinen, R., et al. 1984, *ApJ*, 278, L1
- Nichols, J., Huenemoerder, D. P., Corcoran, M. F., et al. 2015, *ApJ*, 809, 133
- Oplištilová, A., Mayer, P., Harmanec, P., et al. 2023, *A&A*, 672, A31
- Pablo, H., Richardson, N. D., Moffat, A. F. J., et al. 2015, *ApJ*, 809, 134
- Pauwels, T., Reggiani, M., Sana, H., Rainot, A., & Kratter, K. 2023, *A&A*, 678, A172
- Paxton, B., Cantiello, M., Arras, P., et al. 2013, *ApJS*, 208, 4
- Paxton, B., Marchant, P., Schwab, J., et al. 2015, *ApJS*, 220, 15
- Perryman, M. A. C., Lindegren, L., Kovalevsky, J., et al. 1997, *A&A*, 323, L49
- Pietrzyński, G., Graczyk, D., Giallenne, A., et al. 2019, *Nature*, 567, 200
- Prša, A., Conroy, K. E., Horvat, M., et al. 2016, *ApJS*, 227, 29
- Puebla, R. E., Hillier, D. J., Zsargó, J., Cohen, D. H., & Leutenegger, M. A. 2016a, *MNRAS*, 456, 2907
- Puebla, R. E., Hillier, D. J., Zsargó, J., Cohen, D. H., & Leutenegger, M. A. 2016b, *MNRAS*, 456, 2907
- Puls, J., Vink, J. S., & Najarro, F. 2008, *A&A Rev.*, 16, 209
- Renzo, M., Hendriks, D. D., van Son, L. A. C., & Farmer, R. 2022, *Research Notes of the American Astronomical Society*, 6, 25
- Repolust, T., Puls, J., Hanson, M. M., Kudritzki, R. P., & Mokiem, M. R. 2005, *A&A*, 440, 261
- Sana, H., Le Bouquin, J. B., Lacour, S., et al. 2014, *ApJS*, 215, 15
- Sanhueza, P., Jackson, J. M., Zhang, Q., et al. 2017, *ApJ*, 841, 97
- Schaefer, G. H., Hummel, C. A., Gies, D. R., et al. 2016a, *AJ*, 152, 213
- Schaefer, G. H., Hummel, C. A., Gies, D. R., et al. 2016b, *AJ*, 152, 213
- Shenar, T., Oskinova, L., Hamann, W. R., et al. 2015, *ApJ*, 809, 135
- Shenar, T., Sana, H., Mahy, L., et al. 2022, *Nature Astronomy*, 6, 1085
- Sota, A., Maíz Apellániz, J., Morrell, N. I., et al. 2014, *ApJS*, 211, 10
- Taniguchi, Y., Kajisawa, M., Kobayashi, M. A. R., et al. 2015, *Publications of the Astronomical Society of Japan*, 67, 104
- Thompson, G. B. & Morrison, N. D. 2013, *The Astronomical Journal*, 145, 95
- Tokovinin, A., Fischer, D. A., Bonati, M., et al. 2013, *PASP*, 125, 1336
- van Hamme, W. 1993, *AJ*, 106, 2096
- van Leeuwen, F. 2007, *A&A*, 474, 653
- Wilson, R. E., Van Hamme, W., & Terrell, D. 2010, *ApJ*, 723, 1469
- Wongwathanarat, A., Janka, H. T., & Müller, E. 2013, *A&A*, 552, A126

Appendix A: Calibrator of ζ Ori: HIP 26108

The most challenging object for the calibration was ζ Ori because the diameter of its calibrator HIP 26108 in the pipeline database (GRAVI_FAINT_CALIBRATORS.fits) was clearly wrong, and the squared visibility was greater than one in several wavelength intervals. Therefore, we determined the diameter of the calibrator based on the absolute flux from the photometric catalogues in the *VizieR* tool (Allen et al. 2014). We used the standard Johnson system photometry (Ducati 2002) and measurements from Hipparcos (Anderson & Francis 2012), Gaia DR3 (Gaia Collaboration 2020), 2MASS (Cutri et al. 2003), WISE (Cutri et al. 2012), MSX (Egan et al. 2003), SkyMapper (Keller et al. 2007), Subaru/Suprime (Taniguchi et al. 2015), Akari (Ishihara et al. 2010), and IRAS (Neugebauer et al. 1984). The data covered the spectral range from 0.42 to 23.88 μm .

For SED modelling, we used the reddening value $E_{B-V} = 0.014$ mag, i.e. extinction $A_V = 0.0434$ mag (Green et al. 2019)⁶, and the parallax of (6.2 ± 0.1) mas from Gaia, corresponding to $d = (161.1 \pm 2.5)$ pc. Based on the spectral type K4III, we used the temperature $T = 3800$ K and $\log g = 2.0$. The fit with the lowest χ^2 value (see Fig. A.1) led to the physical radius $R = (33.52 \pm 0.53) R_\odot$. We thus recalibrated ζ Ori using the calibrator's angular diameter, $\theta = 2R/d = (1.935 \pm 0.002)$ mas.

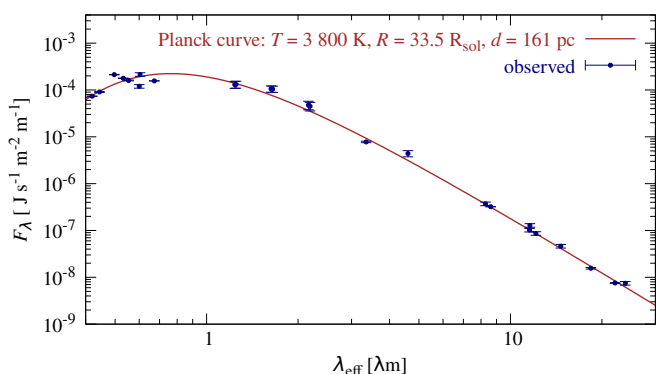


Fig. A.1. SED in terms of the monochromatic flux vs. wavelength for the calibration star HIP 26108, which was used to determine the correct calibrator's radius $R = (33.52 \pm 0.53) R_\odot$ and recalibrate the visibilities of ζ Ori.

Appendix B: Radial velocities

Thompson & Morrison (2013) measured RVs of the He I 6678 \AA lines on 132 electronic spectra from the Ritter Observatory and found variations ranging from about -10 to $+20$ km s^{-1} . In an effort to understand the nature of possible RV changes, we measured RVs of various spectral lines available in the high-resolution spectra at our disposal (CFHT, SOPHIE, and CTIO). The RVs were measured in *reSPEFO*, comparing direct and flipped line profiles on the computer screen. The zero point of the velocity scale was checked via measurements of a selection of telluric lines and also interstellar lines. The results of RV measurements are summarised in Table B.1. It is seen that the individual RVs from spectra taken during a particular observing night agree very well, but there are undoubtedly real RV

Table B.1. Individual radial velocities (in km s^{-1}) measured in the CFHT, SOPHIE, and CTIO electronic spectra.

Line	CFHT	SOPHIE	SOPHIE	CTIO	CTIO
He I 6678 \AA	–	26.8	25.7	9.9	10.5
He I 5876 \AA	21.6	19.7	19.6	5.4	5.4
He I 5015 \AA	22.6	29.6	30.1	17.7	17.5
He I 4922 \AA	22.2	27.1	27.2	15.8	15.5
He I 4713 \AA	21.8	26.7	25.8	16.0	16.4
Si III 4574 \AA	16.6	25.3	23.8	13.9	13.4
Si III 4568 \AA	17.9	25.4	26.2	12.6	12.6
Si III 4552 \AA	20.5	28.4	27.1	12.4	13.8
He II 5411 \AA	29.4	30.7	30.7	26.2	24.1
He II 4686 \AA	42.3	44.7	45.4	35.2	37.6
H β	55.1	50.1	50.5	–22.4	–24.3
H γ	34.5	35.8	33.6	–	–
H δ	31.5	33.1	33.4	–	–
H ϵ	26.3	28.8	28.9	–	–
H8	25.9	–	–	–	–
H9	24.9	–	–	–	–

Notes. Julian dates (UTC) of the observations were 2454754.1558, 2457015.4119, 2457015.4139, 2460637.7725, 2460637.7732.

changes from one observing season to another. We note, however, that the RVs of the He II lines of higher ionisation show little evidence of variability. This seems to contradict the presence of orbital motion in a putative binary system. The observed changes can be caused by some velocity fields in the stellar atmosphere and/or envelope. As Fig. B.1 illustrates, H β line shows variable asymmetry due to partial filling of one or another wing by the emission, which also seems to affect, to some extent, the He I 5876 and 6678 \AA lines. A more systematic study of the nature of these changes seems desirable. At present, we conclude that the single-star models are preferable.

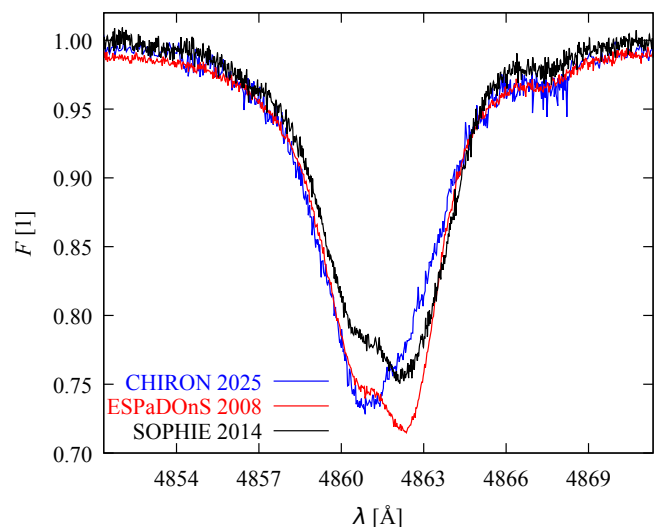


Fig. B.1. The H β line exhibits variable asymmetry due to partial emission filling in one of the wings.

⁶ <http://argonaut.skymaps.info/>

Appendix C: Supplementary tables

In Tab. C.1, SED of ε Ori is summarised.

Table C.1. Absolute monochromatic fluxes for ε Ori. Dereddening was applied to all measurements, assuming $E(B - V) = 0.050$ mag.

λ [Å]	F_λ [$\text{J s}^{-1} \text{m}^{-2} \text{m}^{-1}$]	σ [$\text{J s}^{-1} \text{m}^{-2} \text{m}^{-1}$]	Filter
3531	3.66609 e-02	3.22576 e-03	Johnson:U
3670	3.45552 e-02	7.86573 e-04	Johnson:U, Hvar
4360	1.92305 e-02	5.92874 e-04	Johnson:B, Hvar
4442	1.85143 e-02	1.13899 e-04	Johnson:B
5450	9.07753 e-03	1.49252 e-04	Johnson:V, Hvar
5537	8.64778 e-03	1.36701 e-04	Johnson:V
6730	4.68045 e-03	4.11829 e-04	Gaia:G
6938	4.03631 e-03	3.55151 e-04	Johnson:R
8780	1.64095 e-03	1.44385 e-04	Johnson:I
12 390	4.32121 e-04	9.97331 e-05	2MASS:J
12 500	4.32235 e-04	9.95143 e-05	Johnson:J
16 300	1.32848 e-04	1.91180 e-05	Johnson:H
16 495	1.30820 e-04	1.86919 e-05	2MASS:H
21 638	5.47162 e-05	1.13176 e-05	2MASS:Ks
21 900	5.17698 e-05	1.06892 e-05	Johnson:K

Notes. λ denotes the wavelength; F_λ , the absolute monochromatic flux; and σ , the uncertainty of the absolute flux.

Appendix D: Supplementary figures

We demonstrate the line profiles formation in our model in Figs. D.1 and D.2. Each triangle has a synthetic spectrum, determined by local broadening effects (thermal, pressure, ...). For example, He I and He II lines form at different locations on a fast or critically rotating star due to strong temperature gradients. He I lines have the lowest intensity on the poles, while He II lines have the highest intensity at the poles. For reference, we show the closure phases for the respective model in Fig. D.4.

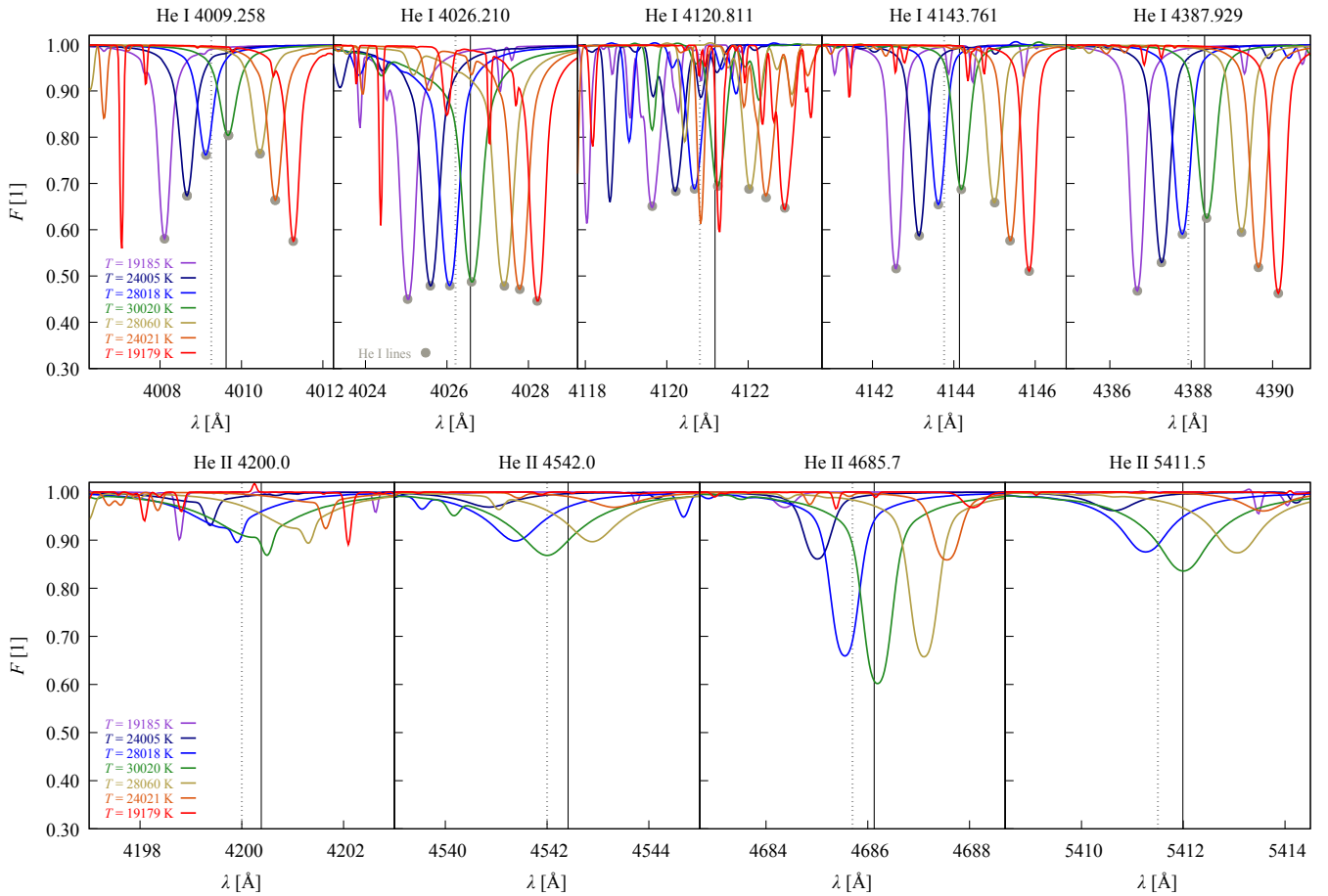


Fig. D.1. Synthetic He I and He II line profiles from our spectroscopic model, corresponding to selected triangles, having a range of temperatures and RVs. For a fast-rotating star, the pole is substantially hotter than the equator. The central line ($RV = 0$) corresponds to the pole, other lines originate from the equator ($RV \neq 0$). He I lines are less intense at the pole, while He II lines are less intense on the equator. The grey points indicate the He I lines for clarity.

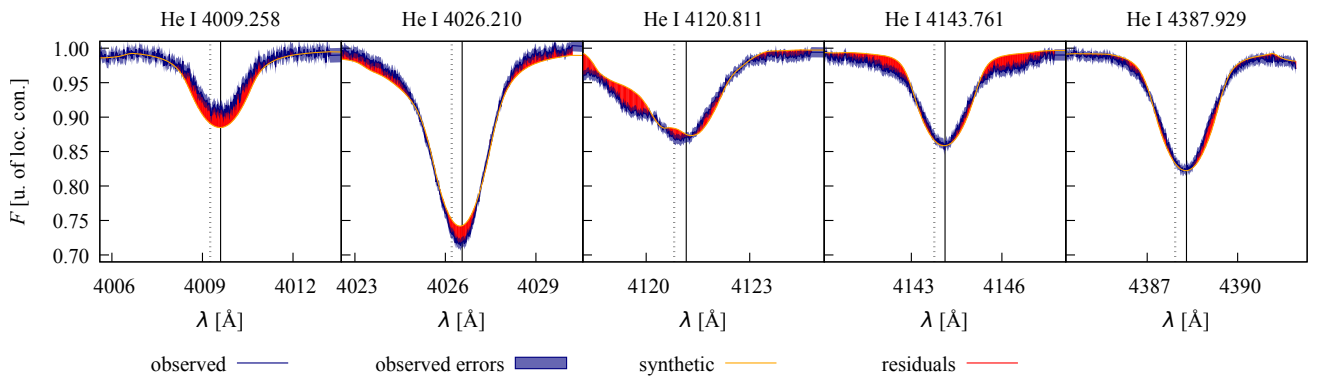


Fig. D.2. Same as Fig. 7 for He I lines. The best-fit spectroscopic model still exhibits systematics (in particular, 4009 and 4026 Å lines). None of these is easy to correct, e.g. by changing T , $\log g$, or metallicity (see also Pablo et al. (2015)).

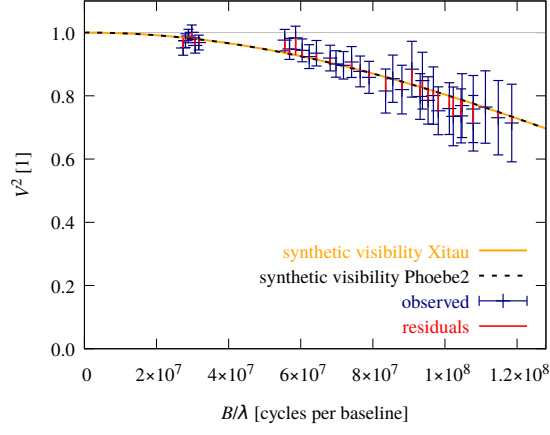


Fig. D.3. Spherical non-rotating model of ε Ori based VLTI/PIONIER observations; the squared visibility vs. the projected baseline B/λ is plotted for two models, Xitau (Brož 2017) and Phoebe (Brož et al. 2025b). The resulting $\chi^2_{\text{VIS}} = 12.1$ is the same in both cases. The number of degrees of freedom, $\nu = N - M = 35$. The resulting parameters are $m = 23.52 M_{\odot}$ (free), $d = 384$ pc (fixed), $T = 27\,000$ K (fixed) (Puebla et al. 2016a), $\log g = 3.0$ (fixed) (Puebla et al. 2016a), $R = 25.40 R_{\odot}$ (derived), $\theta = 0.615$ mas (derived).

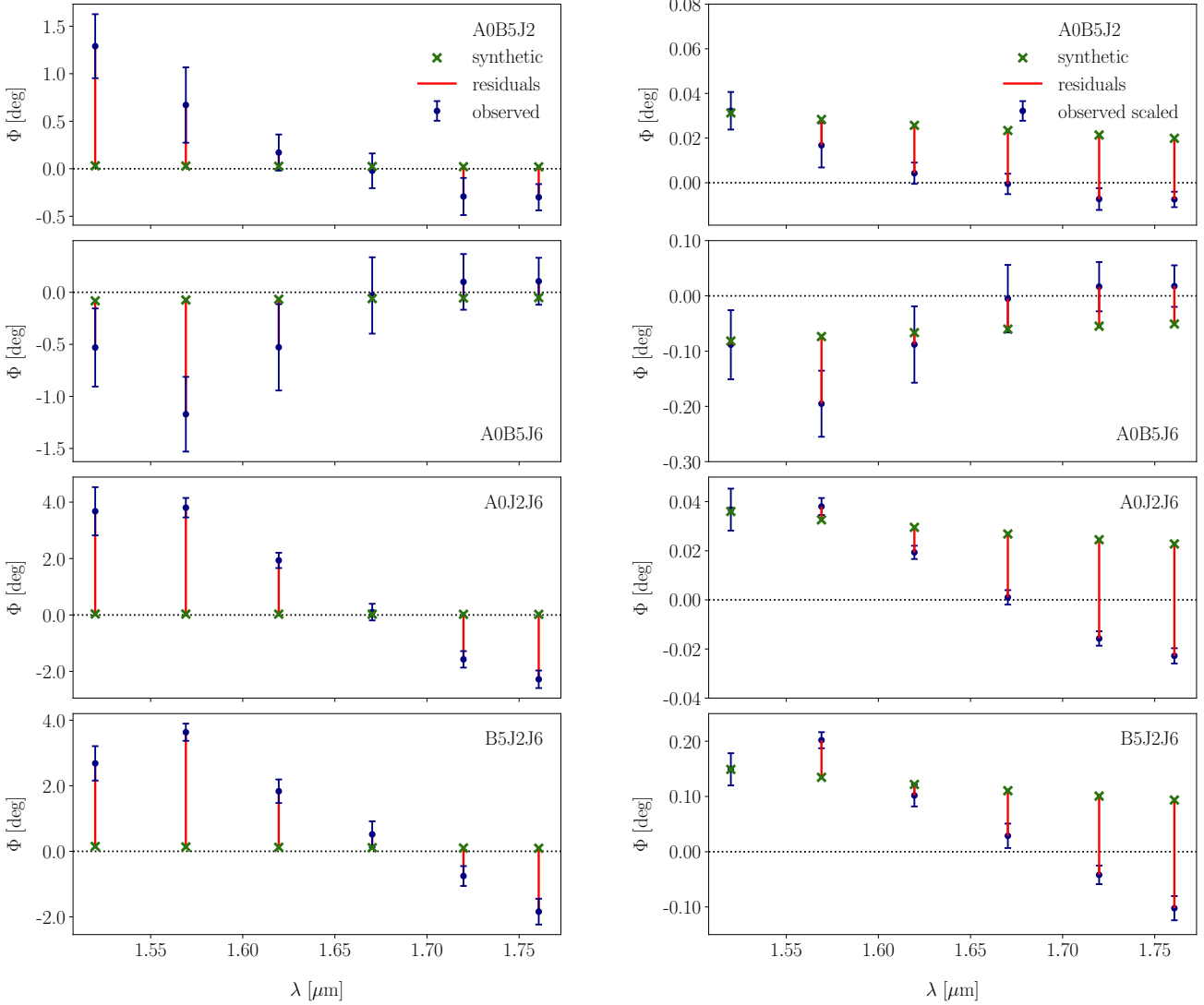


Fig. D.4. Model of ε Ori showing a forward computation of the closure phases with fixed parameters from the visibility model (Fig. 6). The observed closure phases reach up to nearly 4 deg, while the synthetic ones are at most 0.15 deg. If we recalibrate the observed closure phases (left column) by multiplying them by scaling factors 1/40, 1/6, 1/100, and 1/18, respectively for each of the triple baselines (right column), we see similar trends in the observed and synthetic closure phases, $\arg T_3$ vs. B/λ . We used this asymmetry of the flux to set the orientation of the star's equator, as seen by the observer, Ω (favouring 300 deg over 120 deg).